Nonlinear buckling behaviours of thin-walled functionally graded open section beams

Domagoj Lanc[a,*], Goran Turkalj[a] , Thuc P. Vo [b*], Josip Brnić[a]

[a]*Department of Engineering Mechanics, Faculty of Engineering,University of Rijeka, Vukovarska 58, HR-51000 Rijeka, Croatia.*
[b] *Department of Mechanical and Construction Engineering, Northumbria University, Ellison Place, Newcastle upon Tyne, NE1 8ST, UK*

Abstract

In this paper, nonlinear buckling responses of functionally graded (FG) thin-walled open section beams based on Euler-Bernoulli-Vlasov theory is presented.. The finite element incremental equilibrium equations are developed by updated Lagrangian formulation using the non-linear displacement cross-section field that accounts for large rotation effects.. Young's modulus of FG beams are varied continously through the wall thickness based on the power-law distribution. Numerical results are obtained for thin-walled FG beams with symmetric and mono-symmetric I-section and channel-section for various configurations such as boundary conditions, geometry, skin-core-skin ratios and power-law index to investigate the flexural-torsional and lateral buckling loads and post-buckling responses. The accuracy and reliability of proposed model are proved by comparison with previous research and analytical solutions. The importance of above-mentioned effects on buckling results is demonstrated on benchmark examples.

Keywords: Thin-walled FG beams; Finite element; Buckling and post-buckling;

1. Introduction

Thin-walled composite beam structures are widespread in lot of engineering areas due to their high strength-to-weight ratio. Only some of many papers devoted to bending, vibration and buckling of fiber reinforced composite beams-type structures are cited here [1-10]. A development of a new kinds of progressive composites such as functionally graded materials (FGM) in recent years is in a rapid increase. FGMs were first concepted in the late 1980s [11, 12], and after that have been very comprehensively investigated by several researchers. Although many researchers investigated vibration or buckling analysis of FG beams with rectangular cross-section [13-20], thin-walled box section [21] and open section [22, 23], according to the authors' knowledge, there is no work available to study flexural-torsional and lateral

*Corresponding authors
Email addresess: dlanc@riteh.hr (D. Lanc), goran.turkalj@riteh.hr (G. Turkalj), thuc.vo@northumbria.ac.uk (T.P. Vo), brnic@riteh.hr (J. Brnić)

buckling of FG open section beams in a unitary manner. As a result, this is also main objective of this paper. It is based Euler-Bernoulli-Vlasov theory with large displacements and small strains assumptions. Young's modulus of FG beams are varied continuously through the wall thickness according to power-law distribution.. Several doubly-symmetric and mono-symmetric I-section and channel-section beams with different kinds of material distributions are analyzed for buckling under various boundary conditions: clamped-free, simply supported, clamped-simply supported and clamped-clamped. The effects of the geometry, skin-core-skin ratios and power-law index on critical loading and post-buckling respones are investigated.

In this paper, the finite element incremental equilibrium equations are developed by updated Lagrangian formulation using the non-linear displacement cross-section field that accounts for large rotation effects. As an incremental iterative solution scheme, the generalized displacement control method is adopted [24]. At the end of iterations, the nodal orientations updating is carried out using the transformation rule based on the theory of semitangental rotations [25], while so called conventional approach (CA) [26, 27] is performed in the phase of force recovering.

2. Theoretical formulation

In this section, theoretical formulation is briefly summarised and more details of this part can be found in Refs. [10, 21].

2.1. Kinematics

Two sets of are mutually interrelated coordinate systems, which are Cartesian (z, x, y) and contour coordinate system (z, n, s) , are used (Fig. 1).

Cross-sectional displacement incremental values are defined as

$$\begin{aligned} & w_{\mathrm{O}} = w_{\mathrm{O}}(z); \quad u_{\mathrm{S}} = u_{\mathrm{S}}(z); \quad v_{\mathrm{S}} = v_{\mathrm{S}}(z); \quad \varphi_z = \varphi_z(z) \\ & \varphi_x = -\frac{\mathrm{d}v_{\mathrm{S}}}{\mathrm{d}z} = \varphi_x(z); \quad \varphi_y = \frac{\mathrm{d}u_{\mathrm{S}}}{\mathrm{d}z} = \varphi_z(z); \quad \theta = -\frac{\mathrm{d}\varphi_z}{\mathrm{d}z} = \theta(z) \end{aligned} \tag{1}$$

where w_{O} denotes the rigid-body translations of the cross-section centroid in the z-direction and u_{S} and v_{S} are the rigid-body translations in the x- and y-directions associated with shear centre; φ_z, φ_x and φ_y are the rigid-body rotations about the z-, x- and y-shear centre axis, respectively; θ is a cross-section warping parameter.

In the case of small rotations, displacement field is given by [28]:

$$
\begin{aligned}
u_z &= w_{\mathrm{O}} - y\,\frac{\mathrm{d}v_{\mathrm{S}}}{\mathrm{d}z} - x\,\frac{\mathrm{d}u_{\mathrm{S}}}{\mathrm{d}z} - \omega\frac{\mathrm{d}\varphi_z}{\mathrm{d}z} \\
u_x &= u_{\mathrm{S}} - \left(y - y_{\mathrm{S}}\right)\varphi_z \\
u_y &= v_{\mathrm{S}} + \left(x - x_{\mathrm{S}}\right)\varphi_z
\end{aligned}
\tag{2}
$$

in which u_z, u_x and u_y are the first-order (linear) displacement increments of an arbitrary point on the cross-section.

If the large rotation effects are considered, total displacement increments are given by:

$$
u_z + \tilde{u}_z; \quad u_x + \tilde{u}_x; \quad u_y + \tilde{u}_y \tag{3}
$$

where $\tilde{u}_z$, $\tilde{u}_x$, and $\tilde{u}_y$ represent the second-order (non-linear) displacement increments resulting from the large rotations, and expressed by:

$$
\begin{aligned}
\tilde{u}_z &= \frac{1}{2}\left[-\left(x - x_{\mathrm{S}}\right)\varphi_z\,\frac{\mathrm{d}v_{\mathrm{S}}}{\mathrm{d}z} + \left(y - y_{\mathrm{S}}\right)\varphi_z\,\frac{\mathrm{d}u_{\mathrm{S}}}{\mathrm{d}z}\right] \\
\tilde{u}_x &= \frac{1}{2}\left\{-\frac{\mathrm{d}v_{\mathrm{S}}}{\mathrm{d}z}\,\frac{\mathrm{d}u_{\mathrm{S}}}{\mathrm{d}z}\,y - \left[\varphi_z^2 + \left(\frac{\mathrm{d}u_{\mathrm{S}}}{\mathrm{d}z}\right)^2\right]x + x_{\mathrm{S}}\,\varphi_z^2\right\} \\
\tilde{u}_y &= \frac{1}{2}\left\{-\frac{\mathrm{d}v_{\mathrm{S}}}{\mathrm{d}z}\,\frac{\mathrm{d}u_{\mathrm{S}}}{\mathrm{d}z}\,x - \left[\varphi_z^2 + \left(\frac{\mathrm{d}v_{\mathrm{S}}}{\mathrm{d}z}\right)^2\right]y + y_{\mathrm{S}}\,\varphi_z^2\right\}
\end{aligned}
\tag{4}
$$

The Green-Lagrange incremental strain tensor corresponding to the non-linear displacement field from Eq. (3), can be written as:

$$
\varepsilon_{ij} = 0.5\left[\left(u_i + \tilde{u}_i\right)_{,j} + \left(u_j + \tilde{u}_j\right)_{,i} + \left(u_k + \tilde{u}_k\right)_{,i}\left(u_k + \tilde{u}_k\right)_{,j}\right] \cong e_{ij} + \eta_{ij} + \tilde{e}_{ij} \tag{5}
$$

where:

$$
e_{ij} = 0.5\left(u_{i,j} + u_{j,i}\right); \quad \eta_{ij} = 0.5\,u_{k,i}\,u_{k,j}; \quad \tilde{e}_{ij} = 0.5\left(\tilde{u}_{i,j} + \tilde{u}_{j,i}\right) \tag{6}
$$

2.2. Contour displacements

Out of the mid-line displacements are expressed through mid-surface displacements ($\bar{w}$, $\bar{u}$, $\bar{v}$):

$$
w\left(z,s,n\right) = \bar{w} - n\,\frac{\partial \bar{u}}{\partial z}; \quad v\left(z,s,n\right) = \bar{v} - n\,\frac{\partial \bar{u}}{\partial s}; \quad u\left(z,s,n\right) = \bar{u} \tag{7}
$$

Eq. (7) can be seperated into the linear and non-linear parts:

$$
w^L\left(z,s,n\right) = \bar{w}^L - n\,\frac{\partial \bar{u}^L}{\partial z}; \quad v^L\left(z,s,n\right) = \bar{v}^L - n\,\frac{\partial \bar{u}^L}{\partial s}; \quad u^L\left(z,s,n\right) = \bar{u}^L \tag{8}
$$

$$
w^{NL}\left(z,s,n\right) = \bar{w}^{NL} - n\,\frac{\partial \bar{u}^{NL}}{\partial z}; \quad v^{NL}\left(z,s,n\right) = \bar{v}^{NL} - n\,\frac{\partial \bar{u}^{NL}}{\partial s}; \quad u^{NL}\left(z,s,n\right) = \bar{u}^{NL} \tag{9}
$$

where

$$\begin{aligned}
&\bar{w}^{L} = u_z(z,s,n); \quad \bar{w}^{NL} = \tilde{u}_z(z,s,n);\\
&\bar{v}^{L} = u_x(z,s,n)\cos\beta + u_y(z,s,n)\sin\beta; \quad \bar{v}^{NL} = \tilde{u}_x(z,s,n)\cos\beta + \tilde{u}_y(z,s,n)\sin\beta;\\
&\bar{u}^{L} = u_x(z,s,n)\sin\beta - u_y(z,s,n)\cos\beta; \quad \bar{u}^{NL} = \tilde{u}_x(z,s,n)\sin\beta - \tilde{u}_y(z,s,n)\cos\beta
\end{aligned} \tag{10}$$

and the superscripts *NL* and *L* indicate the nonlinear and linear parts.

Non-zero strains are given by [29]:

$$e_{zz} = \frac{\partial w^{L}}{\partial z}; \quad e_{zs} = \frac{\partial w^{L}}{\partial s} + \frac{\partial v^{L}}{\partial z}; \tag{11}$$

$$\eta_{zz} = \frac{1}{2}\left[\left(\frac{\partial w^{L}}{\partial z}\right)^2 + \left(\frac{\partial u^{L}}{\partial z}\right)^2 + \left(\frac{\partial v^{L}}{\partial z}\right)^2\right]; \quad \eta_{zs} = \frac{\partial w^{L}}{\partial z}\frac{\partial w^{L}}{\partial s} + \frac{\partial u^{L}}{\partial z}\frac{\partial u^{L}}{\partial s} + \frac{\partial v^{L}}{\partial z}\frac{\partial v^{L}}{\partial s}; \tag{12}$$

$$\tilde{e}_{zz} = \frac{\partial w^{NL}}{\partial z}; \quad \tilde{e}_{zs} = \frac{\partial w^{NL}}{\partial s} + \frac{\partial v^{NL}}{\partial z} \tag{13}$$

where, e_{ij} and η_{ij} are the linear and non-linear strain components corresponding to the first-order displacements, while $\tilde{e}_{ij}$ is the linear strain component corresponding to the second-order "large rotation" displacements.

After substitution of Eq. (8) into Eq. (11), follows:

$$e_{zz} = \frac{\partial w^{L}}{\partial z} = \frac{\partial \bar{w}^{L}}{\partial z} - n\frac{\partial^2 \bar{u}^{L}}{\partial z^2} = \bar{\varepsilon}_z^{\,L} + n\kappa_z^{\,L} \tag{14}$$

$$e_{zs} = \frac{\partial w^{L}}{\partial s} + \frac{\partial v^{L}}{\partial z} = -2n\frac{\partial^2 \bar{u}^{L}}{\partial s \partial z} = n\kappa_{zs}^{\,L} \tag{15}$$

where

$$\bar{\varepsilon}_z^{\,L} = \frac{\partial \bar{w}^{L}}{\partial z} = \frac{\mathrm{d}w_{\mathrm{O}}}{\mathrm{d}z} - y\frac{\mathrm{d}^2 v_{\mathrm{S}}}{\mathrm{d}z^2} - x\frac{\mathrm{d}^2 u_{\mathrm{S}}}{\mathrm{d}z^2} - \omega\frac{\mathrm{d}^2 \varphi_z}{\mathrm{d}z^2} \tag{16}$$

$$\kappa_z^{\,L} = -\frac{\partial^2 \bar{u}}{\partial z^2} = -\frac{\mathrm{d}^2 u_{\mathrm{S}}}{\mathrm{d}z^2}\sin\beta + \frac{\mathrm{d}^2 v_{\mathrm{S}}}{\mathrm{d}z^2}\cos\beta + \frac{\mathrm{d}^2 \varphi_z}{\mathrm{d}z^2} q \tag{17}$$

$$\kappa_{zs}^{\,L} = 2\frac{\mathrm{d}\varphi_z}{\mathrm{d}z} \tag{18}$$

where *r* and *q* represent the contour radius and the shear centre normal distance of the contour radius, and warping function ω with the respect to contour coordinate system is given [30] (Fig. 1):

$$r = (x - x_{\mathrm{S}})\sin\beta - (y - y_{\mathrm{S}})\cos\beta \tag{19}$$

$$q = (y - y_{\mathrm{S}})\sin\beta + (x - x_{\mathrm{S}})\cos\beta \tag{20}$$

$$\omega = \int_s r\, ds; \tag{21}$$

Eqs. (14) and (15) can be rewritten as:

$$e_{zz} = \varepsilon_z^0 + \kappa_x(y - n\cos\beta) + \kappa_y(x + n\sin\beta) + \kappa_\omega(\omega - nq) \tag{22}$$

$$e_{zs} = n\kappa_{sz} \tag{23}$$

where the ε_z^0 - axial strain, κ_x - and κ_y - the biaxial curvatures in *x* and *y* direction, κ_ω - warping curvature and κ_{sz} - twisting curvature, are defined as:

$$\varepsilon_z^0 = \frac{\mathrm{d}w_O}{\mathrm{d}z}; \quad \kappa_y = -\frac{\mathrm{d}^2 u_S}{\mathrm{d}z^2}; \quad \kappa_x = -\frac{\mathrm{d}^2 v_S}{\mathrm{d}z^2}; \quad \kappa_\omega = -\frac{\mathrm{d}^2 \varphi_z}{\mathrm{d}z^2}; \quad \kappa_{sz} = 2\frac{\mathrm{d}\varphi_z}{\mathrm{d}z}. \tag{24}$$

2.3. Stress resultants

The internal stress resultants (F_z, M_x, M_y, M_T and M_ω) can be defined as:

$$F_z = \int_A \sigma_z\, dn\, ds, \quad M_x = \int_A \sigma_z (y - n\cos\beta) dn ds,$$

$$M_y = \int_A \sigma_z (x + n\sin\beta) dn ds, \quad M_T = \int_A \tau_{zs} n\, dn ds,$$

$$M_\omega = \int_A \sigma_z (\omega - nq) dn ds, \quad \bar{K} = \int_A \sigma_z \left[(x - x_s)^2 + (y - y_s)^2 \right] dn ds \tag{25}$$

In Eq. (24), $\bar{K}$ is the Wagner coefficient defined as [28]:

$$\bar{K} = F_z\alpha_z + M_x\alpha_x + M_y\alpha_y + M_\omega\alpha_\omega \tag{26}$$

where:

$$\alpha_z = \frac{I_x + I_y}{A} + x_s^2 + y_s^2, \quad \alpha_x = \frac{1}{I_x}\int_A (x^2 y + y^3) dA - 2y_s,$$
$$\alpha_y = -\frac{1}{I_y}\int_A (x^3 + xy^2) dA + 2x_s, \quad \alpha_\omega = \frac{1}{I_\omega}\int_A (x^2 + y^2)\omega dA, \tag{27}$$

with A as an area, I_x and I_y as a second moments of area about principal *x*- and *y*-axis, and I_ω as a warping constant of cross-section.

2.4. Stress-strain relations

For simplicity, Poisson's ratio v, is assumed to be constant, whereas, Young's modulus is varied continuously through the wall thickness according to power-law distribution [31]:

$$E(n) = \left(E_{top} - E_{bot}\right) \cdot V_c + E_{bot} \tag{28}$$

where subscripts *top* and *bot* indicate the top and bottom surface components, and V_c represent the volume fraction of the ceramic phase, respectively. Three variants of FG beam walls are considered [21] (Fig. 2):

1) Type A: the wall is graded from metal surface ($n = t_0 = -t/2$) to a top ceramic surface ($n = t_3 = +t/2$) and V_c can be given by:

$$V_c = \left(\frac{1}{2} + \frac{n}{t}\right)^p, \qquad t_0 \le n \le t_3 \tag{29}$$

2) Type B: the wall is made of ceramic core and FG skins. The top skin varies from a fully ceramic ($n = t_2$) to a fully metal surface ($n = t_3 = +t/2$) while the bottom skin varies from a fully metal ($n = t_0 = -t/2$) to a fully ceramic surface ($n = t_1$). V_c can be determinated as:

$$\begin{aligned} V_c &= \left(\frac{n - t_3}{t_2 - t_3}\right)^p, && t_2 \le n \le t_3 \\ V_c &= 1, && t_1 \le n \le t_2 \\ V_c &= \left(\frac{n - t_0}{t_1 - t_0}\right)^p, && t_0 \le n \le t_1 \end{aligned} \tag{30}$$

3) Type C: the bottom is graded from fully metal to fully ceramic the while the top skin is entirely ceramic [22]. V_c can be determinated as:

$$\begin{aligned} V_c &= \left(\frac{n - t_0}{t_2 - t_0}\right)^p, && t_0 \le n \le t_2 \\ V_c &= 1, && t_2 \le n \le t_3 \end{aligned} \tag{31}$$

where p is the power-law index.

The constitutive equations for thin-walled FG beams can be expressed as:

$$\sigma_z = E(n) \cdot \varepsilon_z, \qquad \tau_{zs} = \frac{E(n)}{2\left[1 + \nu(n)\right]} \cdot \gamma_{zs} = G(n) \cdot \gamma_{zs} \tag{32}$$

Using Eqs. (22), (23) and (32), the beam forces can be written as:

$$\left.\begin{aligned} F_z &= R_{11}\varepsilon_z^0 + R_{12}\kappa_y + R_{13}\kappa_x + R_{14}\kappa_\omega \\ M_y &= R_{12}\varepsilon_z^0 + R_{22}\kappa_y + R_{23}\kappa_x + R_{24}\kappa_\omega \\ M_x &= R_{13}\varepsilon_z^0 + R_{23}\kappa_y + R_{33}\kappa_x + R_{34}\kappa_\omega \\ M_\omega &= R_{14}\varepsilon_z^0 + R_{24}\kappa_y + R_{34}\kappa_x + R_{44}\kappa_\omega \\ M_T &= R_{55}\kappa_{sz} \end{aligned}\right\} \tag{33}$$

where R_{ij} are thin-walled FG beam rigidities:

$$\left.\begin{aligned} R_{11} &= \int_A E(n)\,dn\,ds, \quad R_{12} = \int_A E(n)\,x\,dnds + \int_A E(n)\,n\sin\beta\,dnds, \\ R_{13} &= \int_A E(n)\,y\,dnds - \int_A E(n)\,n\cos\beta\,dnds, \quad R_{14} = \int_A E(n)\,\omega\,dnds - \int_A E(n)\,n\,q\,dnds, \\ R_{22} &= \int_A E(n)\,x^2\,dnds - 2\int_A E(n)\,n\,x\sin\beta\,dnds + \int_A E(n)\,n^2\sin^2\beta\,dnds, \\ R_{23} &= \int_A E(n)\,xy\,dnds + \int_A E(n)\,n\,(y\sin\beta - x\cos\beta)\,dnds - \int_A E(n)\,n^2\sin\beta\cos\beta\,dnds, \\ R_{24} &= \int_A E(n)\,x\omega\,dnds + \int_A E(n)\,n\,(\omega\sin\beta - xq)\,dnds - \int_A E(n)\,n^2\,q\sin\beta\,dnds, \\ R_{33} &= \int_A E(n)\,y^2\,dnds - 2\int_A E(n)\,n\,y\cos\beta\,dnds + \int_A E(n)\,n^2\cos^2\beta\,dnds, \\ R_{34} &= \int_A E(n)\,y\omega\,dnds - \int_A E(n)\,n\,(\omega\cos\beta + yq)\,dnds + \int_A E(n)\,n^2\,q\cos\beta\,dnds, \\ R_{44} &= \int_A E(n)\,\omega^2\,dnds - 2\int_A E(n)\,n\,q\omega\,dnds + \int_A E(n)\,n^2q^2dnds, \quad R_{55} = \int_A G(n)\,n^2dnds \end{aligned}\right\} \tag{34}$$

2.5. Centre of gravity and shear centre

According to definition in Refs. [22, 32], the center of gravity (x_0, y_0) is described as the axial force application point, the acting point of axial stresses resultant caused by a constant state of strains ε_z^0. From moments equality with respect to the *x* and *y* axes:

$$F_z \cdot y_0 = M_x, \quad F_z \cdot x_0 = M_y \tag{35}$$

and Eq. (33) the center of gravity coordinates can be determinated as:

$$x_0 = -\frac{\overline{R}_{12}}{R_{11}}, \quad y_0 = \frac{\overline{R}_{13}}{R_{11}} \tag{36}$$

where

$$\overline{R}_{12} = \int_A E(n)\,(\overline{x} + n\sin\beta)dnds\,, \tag{37}$$

$$\overline{R}_{13} = \int_A E(n)(\overline{y} - n\cos\beta)dnds\,, \tag{38}$$

with the $\overline{x}$ and $\overline{y}$ as a coordinates from the origin.

Assuming the FG beam is under torsion only, the bending moments are equal zero:

$$M_x = R_{34}^0 - x_s R_{33} + y_s R_{23} = 0 \tag{39}$$

$$M_y = R_{24}^0 - x_s R_{23} + y_s R_{22} = 0 \tag{40}$$

And the shear centre coordinates will be:

$$x_s = \frac{R_{22}R_{34}^0 - R_{23}R_{24}^0}{R_{22}R_{33} - R_{23}R_{23}}, \qquad y_s = -\frac{R_{33}R_{24}^0 - R_{23}R_{34}^0}{R_{22}R_{33} - R_{23}R_{23}} \tag{41}$$

In expressions above, the index O denotes the values with respect to centre of gravity [32].

3. Finite element formulation

The 14 degree of freedom beam finite element is shown on Fig. 3, defined in local element coordinate system (z, x, y). The nodal displacement and force vectors are following:

$$\mathbf{u}^e = \begin{Bmatrix} \mathbf{u}_{\mathrm{A}}^e \\ \mathbf{u}_{\mathrm{B}}^e \end{Bmatrix}; \quad \left(\mathbf{u}_i^e\right)^{\mathrm{T}} = \begin{Bmatrix} w_i & u_i & v_i & \varphi_{zi} & \varphi_{xi} & \varphi_{yi} & \theta_i \end{Bmatrix}, \quad i = \mathrm{A, B} \tag{42}$$

$$\mathbf{f}^e = \begin{Bmatrix} \mathbf{f}_{\mathrm{A}}^e \\ \mathbf{f}_{\mathrm{B}}^e \end{Bmatrix}; \quad \left(\mathbf{f}_i^e\right)^{\mathrm{T}} = \begin{Bmatrix} F_{zi} & F_{xi} & F_{yi} & M_{zi} & M_{xi} & M_{yi} & M_{\omega i} \end{Bmatrix}, \quad i = \mathrm{A, B}. \tag{43}$$

The superscript *e* denotes the eth finite element. The rotational degrees of freadom φ_{xi}, and φ_{yi}, from Eq. (42), as well as the warping parameters θ_i (i = A, B) are specified in Eq. (1).

By applying the principle of virtual work, the beam element incremental equilibrium equations in linearized form follows as:

$$\delta \mathsf{U}_{\mathrm{E}} + \delta \mathsf{U}_{\mathrm{G}} = \delta^2 \mathsf{W} - \delta^1 \mathsf{W} \tag{44}$$

where the internal work from the left-hand side is compounded of the incremental virtual elastic strain energy:

$$\delta \mathsf{U}_{\mathrm{E}} = \int_{^1V} {}_1C_{ijkl}\, {}_1e_{kl}\, \delta\, {}_1e_{ij}\, {}^1\mathrm{d}V \tag{45}$$

and the incremental virtual geometric potential:

$$\delta \mathsf{U}_{\mathrm{G}} = \int_{^1V} {}^1S_{ij}\, \delta_1\eta_{ij}\, {}^1\mathrm{d}V + \int_{V} {}^1S_{ij}\, \delta_1\tilde{e}_{ij}\, {}^1\mathrm{d}V - \int_{^1A_\sigma} {}^1t_i\, \delta\tilde{u}_i\, {}^1\mathrm{d}A_\sigma\,. \tag{46}$$

The right-hand side terms present the virtual work carried out by the external forces at the end and at the beginning of the increment,

$$\delta^2 \mathsf{W} = \int_{^1A_\sigma} {}^2t_i \, \delta u_i \, {}^1\mathrm{d}A_\sigma \,, \quad \delta^1 \mathsf{W} = \int_{^1V} {}^1S_{ij} \, \delta_1 e_{ij} \, {}^1\mathrm{d}V = \int_{^1A_\sigma} {}^1t_i \, \delta u_i \, {}^1\mathrm{d}A_\sigma \tag{47}$$

where S_{ij} is second of Piola-Kirchhoff stress tensor, t_i denotes the surface tractions, C_{ijkl} is the stress-strain tensor. Applying a linear interpolation functions for w_i and a cubic ones for u_i, v_i and φ_z one can get:

$$\delta \mathsf{U}_\mathrm{E} = \int_V S_{ij} \, \delta e_{ij} \, \mathrm{d}V = \left(\delta \mathbf{u}^\mathrm{e}\right)^\mathrm{T} \mathbf{k}_\mathrm{E}^\mathrm{e} \, \mathbf{u}^\mathrm{e}, \tag{48}$$

$$\delta \mathsf{U}_\mathrm{G} = \int_V S_{ij} \left(\delta \eta_{ij} + \delta \tilde{e}_{ij}\right) \mathrm{d}V - \int_{A_\sigma} t_i \, \delta \tilde{u}_i \, \mathrm{d}A_\sigma = \left(\delta \mathbf{u}^\mathrm{e}\right)^\mathrm{T} \mathbf{k}_\mathrm{G}^\mathrm{e} \, \mathbf{u}^\mathrm{e}, \tag{49}$$

$$\delta \mathsf{W} = \int_V S_{ij} \, \delta e_{ij} \, \mathrm{d}V = \left(\delta \mathbf{u}^\mathrm{e}\right)^\mathrm{T} \mathbf{f}^\mathrm{e}. \tag{50}$$

where $\mathbf{f}^\mathrm{e}$ is a nodal force vector, $\mathbf{k}_\mathrm{E}^\mathrm{e}$ denotes the elastic stiffness matrix and $\mathbf{k}_\mathrm{G}^\mathrm{e}$ is the geometric stiffness matrix, respectively. It is worth noting that terms arising from the nonlinear components completely coincide with the expressions already derived in the literature [33].

An incremental iterative approach should be dealt with the set of non-linear equilibrium equations established for whole structure. The procedure adopted in this work is the one previously detailed described in [26].

4. Numerical examples

The buckling analysis is performed for seven types of FG beam cross section: two types of symmetric I-sections (I1 and I2), two types of monosymetric I-sections (M1, M2) and three types of channel sections (C1, C2, C3). The letters A, B and C denotes three types of beam walls (see Fig. 4), while the numbers next to denote the skin-core-skin ratios (Table 1). For all beams the web heights are h = 0.2 m and the thicknesses of the wall are t = 0.005 m. The flange widths for I- and C-type beams are b = 0.1 m, while for M-type cross sections, the flange widths are b_{top} = 0.1 m, b_{bot} = 0.05 m. The material parameters are: E_c = 320.7 GPa, E_m = 105.69 GPa, $\nu_\mathrm{m} = \nu_\mathrm{c} = 0.3$.

For verification purpose, the model is firstly tested on static response of cantilevered FG thin-walled beams with length L=2.5 m and various cross sections. The results obtained for non-dimensional deflections $\overline{V} = V E_c t h^3 / F_y L^3$ and twist angles $\overline{\Phi} = \Phi G_c h t^3 / M_z L^3$ are compared with

those of Nguyen et al. [22] in Figs. 5 and 6. A very good correlation is observed for entire set of cross-sections and power-law index values.

4.1. Flexural-torsional buckling

The buckling loads of FG beams with length L=2.5 m and various power-law index p for different types of boundaries, simply supported (S-S), clamped-free (C-F), clamped-clamped (C-C) and clamped-simply supported (C-S), are given in Tables 2-8. For verification purposes, the results are also analytically obtained as the roots of following cubic formula [34]:

$$F^2\left[\left(F-F_y\right)x_s^2+\left(F-F_x\right)y_s^2\right]-\frac{I_{ps}}{A}\left(F-F_x\right)\left(F-F_y\right)\left(F-F_\varphi\right)=0 \tag{51}$$

where:

$$F_x=\frac{\pi^2 R_{33}}{\left(kL\right)^2},\qquad F_y=\frac{\pi^2 R_{22}}{\left(kL\right)^2},\qquad F_\varphi=\frac{A}{I_{ps}}\left(4R_{55}+\frac{\pi^2 R_{44}}{\left(kL\right)^2}\right) \tag{52}$$

are the critical buckling loads about the x and y axes, as well as the critical buckling load for purely torsional buckling, respectively. The I_{ps} denotes the polar moment of inertia about the shear centre:

$$I_{ps}=I_x+I_y+A\left(x_s+y_s\right) \tag{53}$$

while the k is theoretical value of effective-length factor which is dependent on boundary conditions.

Due to symmetric in both geometry and material distribution in the case of I1 and I2 beam types, the shear centre is coincident with the centroid. In these cases, the lowest buckling modes corresponds to flexural ones in weaker direction and the critical buckling loads are equal to F_y. In the case of M1, M2, C1, C2 and C3, the corresponding buckling modes are torsional-flexural and the critical load, the smallest of three roots of Eq. (51), is less then all three values from Eq. (52). Since the present results satisfactorily match the analytical ones, the accuracy of proposed model is again established. It can be noticed that how the power-law index increases it causes a reduction in Young's modulus which results in the reduction of buckling loads. One can notice that the distribution of material has a major impact on buckling load of all beams for all four observed boundary conditions.

With the intension to indicate the robustness and stability of used algorithm, the responses of C2 and C3 cantilever beams are further investigated in the nonlinear manner. A small perturbing force ΔF = 0.001 F is applied laterally at free end to stimulate buckling. The obtained curves represent the axial force *vs*

displacements of point at which the perturbation force acts, Fig. 7. The result are given for power-law index values p = 0.25 and p = 2. These load-deflection curves match well with buckling loads obtained previously in eigenvalue manner. It is manifested as a sharp rise of lateral deflection as the load approaches the critical buckling value.

4.2. Lateral buckling

The model is further tested for lateral buckling of simply-supported beams with length L = 8 m, for various types of loading: pure bending, mid-span point load and uniformly distributed loading. The loadings are applied at shear centre. For verification purposes, results from an isotropic case of pure ceramic are firstly calculated to compare with those from closed form solutions [34-36]:

Pure bending:

$$\begin{aligned} M_{cr1} &= \frac{\pi}{L}\sqrt{EI_y GJ}\sqrt{1+\frac{\pi^2 EI_\omega}{L^2 GJ}} \quad \text{for I and C-sections} \\ M_{cr2} &= M_{cr1}\cdot\sqrt{1+\left(\frac{\alpha_x\cdot F_y}{2M_{cr1}}\right)^2}+0.5(\alpha_x\cdot F_y) \quad \text{for M-sections} \end{aligned} \tag{54}$$

Uniformly distributed load:

$$\begin{aligned} q_{cr1} &= f_q\frac{\sqrt{EI_y GJ}}{L^3} \quad \text{for I and C-sections} \\ q_{cr2} &= \frac{9.04M_{cr1}}{L^2}\cdot\sqrt{1+0.06638\left(\frac{\alpha_x\cdot F_y}{M_{cr1}}\right)^2}+\frac{2.32907\alpha_x\cdot F_y}{L} \quad \text{for M-sections} \end{aligned} \tag{55}$$

Central point load:

$$\begin{aligned} F_{cr1} &= f_F\frac{\sqrt{EI_y GJ}}{L^2} \quad \text{for I and C-sections} \\ F_{cr2} &= \frac{5.4M_{cr1}}{L}\cdot\sqrt{1+0.03885\left(\frac{\alpha_x\cdot F_y}{M_{cr1}}\right)^2}+\frac{1.06434\alpha_x\cdot F_y}{L} \quad \text{for M-sections} \end{aligned} \tag{56}$$

In Eqs. (55) and (56), the f_q and f_F are coefficient factors defined in [34, 35] and J denotes St. Venant torsional constant, while α_x is Wagner coefficient factor defined in Eq. (27).

It should be noted that the lateral buckling moments are assumed to be positive, which means that such moments cause tension in the top flange. It is seen from Table 9. that the present results are in excellent agreement with the closed form solutions. The eigenvalue results of buckling loads versus power-law index

for seven types of FG beams are plotted in Figs. 8-10. Responses evaluated using load-deflection manner are illustrated for M1 and M2 cross sections with power law exponent $p = 5$. A small perturbation twisting moment $\Delta M = 0.01M$ is applied at mid span for pure bending, perturbation force $\Delta F = 0.001qL$ for uniform loading and perturbation twisting moment $\Delta M = 0.00125FL$ for concentrated force loading case. Figs. 11-13 represent lateral displacement *vs* applied moment M for pure bending and lateral displacement *vs* applied uniform loading q, as well as lateral displacement *vs* applied concentrated force F, respectively.

In order to further investigate lateral buckling responses, a L-shaped frame with channel cross section under horizontal load is analyzed, Fig. 14. This frame is fixed at point A and loaded at point C in X direction passing through the shear centre. The length of both frame legs is $L = 2.5$m while cross section is considered to be of C2 and C3 types. The warping condition at point B is considered as completely restrained. For two different directions of load, (+) and (-), the obtained results for the critical buckling loads are given in Table 10 and plotted in Fig. 15. For the goal of result validationon, the buckling loads for purely ceramic cross section are calculated by NASTRAN shell model [37]. The obtained values $(-)F_{cr} = 0.021176$ MN and $(+)F_{cr} = 0.022895$ MN are agree well with the present results corresponding to $p = 0$ obtained from the proposed model. The corresponding lateral modes are illustrated on Fig. 16. In the load-deflection manner obtained curves representing the lateral displacements at point C versus applied load acting in positive direction. These results are plotted for power-law index $p = 0.25$ and $p = 2$, Figs. 17 and 18. Lateral disturbing force $\Delta F = 0.001\ F$ is added at free end in negative Z direction. Very good recognition of critical buckling values is remarked.

5. Conclusion

A beam model for non-linear buckling analysis of thin-walled functionally graded open section beam-type structures is presented. The finite element incremental equilibrium equations have been developed by UL formulation using the non-linear displacement cross-section field that accounts for large rotation effects. Three variants of beam wall are investigated: Type A - FG wall, Type B - sandwich wall with two FG skins and homogeneous ceramic core and Type C - sandwich wall with homogenious ceramic skin and FG core. Also, three types of cross sections are considered: symmetric and mono-symetric I- and channel section. For various boundary conditions, the influence of power law index magnitude on the critical buckling loads and post-buckling responses are observed as well as the effects of skin-core-skin thickness ratios. Variation

of the center of gravity and shear center positions depending on material distribution is also taken into account. The effeciency of the proposed algorithm has been tested considering some benchmark examples.

Acknowledgement

The authors gratefully acknowledge financial support from Croatian Science Foundation under (project No. 6876) and University of Rijeka (13.09.1.1.03 and 13.09.2.2.20).

References

[1] Lee J, Kim SE, Hong K. Lateral buckling I-section beams. Engineering Structures, 2002; 24: 955–964.

[2] Lee J: Flexural analysis of thin-walled composite beams using shear-deformable beam theory. Composite Structures, 2005; 70: 212-222.

[3] Cardoso JEB, Benedito NMB, Valido AJJ. Finite element analysis of thin-walled composite laminated beams with geometrically nonlinear behavior including warping deformation. Thin-Walled Structures, 2009; 47: 1363-1372.

[4] Silva NF, Silvestre N. On the Influence of Material Couplings on the linear and Buckling Behavior if I-section Composite Columns. International Journal of Structural Stability and Dynamics, 2007; 7: 243–272

[5] Vo TP, Lee J, Ahn N. On sixfold coupled buckling of thin-walled composite beams. Composite structures, 2009; 90(3): 295-303.

[6] Cortinez VH, Piovan MT. Stability of composite thin-walled beams with shear deformability. Computers & Structures, 2006; 84: 978-990.

[7] Carrera, E, Filippi, M, Zappino, E. Laminated beam analysis by polynomial, trigonometric, exponential and zig-zag theories. Europian Journal of Mechanics – A/Solids, 2013; 41: 58–69.

[8] Vo, TP, Lee, J. Geometrically nonlinear analysis of thin-walled open-section composite beams. Computers & Structures, 2010; 88: 347-356.

[9] Filippi M, Pagani A, Petrolo M , Colonna G, Carrera E, Static and free vibration analysis of laminated beams by refined theory based on Chebyshev polynomials, Composite Structures, 2015; 132, 1248-1259.

[10] Lanc D, Turkalj G, Pesic I. Global buckling analysis model for thin-walled composite laminated beam

type structures. Composite Structures, 2014; 111: 371-380.

[11] Shen HS, Functionally Graded Materials, Nonlinear Analysis of Plates and Shells, CRC Press, 2009.

[12] Tornabene F, Fantuzzi N, Bacciocchi M , Free vibrations of free-form doubly-curved shells made of functionally graded materials using higher-order equivalent single layer theories, Composites Part B: Engineering, 2014; 67: 490-509

[13] Chakraborty A, Gopalakrishnan S, Reddy JN, A new beam finite element for the analysis of functionally graded materials, International Journal of Mechanical Sciences, 2003; 45 (3): 519 –539.

[14] Vo TP, Thai H-T, Nguyen T-K, Maheri A, Lee J, Finite element model for vibration and buckling of functionally graded sandwich beams based on a refined shear deformation theory, Engineering Structures, 2014; 64: 12 – 22.

[15] Ziane N, Meftah SA, Belhadj HA, Tounsi A, Bedia EAA, Free vibration analysis of thin and thick-walled FGM box beams, International Journal of Mechanical Sciences 66 (2013) 273 – 282.

[16] Sina SA, Navazi HM, Haddadpour H, An analytical method for free vibration analysis of functionally graded beams, Materials & Design, 2009; 30 (3): 741 – 747.

[17] Simsek M, Fundamental frequency analysis of functionally graded beams by using different higher-order beam theories, Nuclear Engineering and Design, 2010; 240 (4): 697 – 705.

[18] Alshorbagy AE, Eltaher M, Mahmoud F, Free vibration characteristics of a functionally graded beam by finite element method, Applied Mathematical Modelling, 2011; 35 (1): 412 – 425.

[19] Mantari JL, Yarasca J, A simple and accurate generalized shear deformation theory for beams, Composite Structures, 2015; 134: 593-601.

[20] Vo TP, Thai H-T, Nguyen T-K, Inam F, Static and vibration analysis of functionally graded beams using refined shear deformation theory, Meccanica, 2013: 1–14.

[21] Lanc D, Vo TP, Turkalj G, Lee J, Buckling analysis of thin-walled functionally graded sandwich box beams, Thin-Walled Structures, 2015; 86: 148-156.

[22] Nguyen T-T, Kim N-II, Lee J, Analysis of thin-walled open-section beams with functionally graded materials, Composite Structures, 2016; 138: 75-83.

[23] Nguyen T-T, Kim N-II, Lee J, Free vibration of thin-walled functionally graded open-section beams, Composites Part B, 2016; 95: 105-116.

[24] Yang, YB, Kuo, SR. Theory & Analysis of Nonlinear Framed Structures. New York: Prentice Hall; 1994.

[25] Argyris, JH, Dunne, PC, Scharpf, DW. On large displacement-small strain analysis of structures with rotational degrees of freedom. Computer Methods in Applied Mechanics and Engineering, 1978; 14: 401-451.

[26] Turkalj, G, Brnic, J, Kravanja, S. A beam model for large displacement analysis of flexibly connected thin-walled beam-type structures. Thin-Walled Structures, 2011; 49:1007-1016.

[27] McGuire, W, Gallagher, RH, Ziemian, R. Matrix Structural Analysis. New York: John Wiley & Sons; 2000.

[28] Chen WF, Atsuta T. Theory of beam–columns. Vol. 2: Space behavior and design, J. Ross Publishing, Fort Lauderdale; 2008.

[29] Turkalj G, Lanc D, Brnić J, Pešić I, A beam formulation for large displacement analysis of composite frames with semi-rigid connections, Composite Structures, 2015; 134: 237-246.

[30] Gjelsvik, A. The Theory of Thin Walled Bars. New York; Wiley; 1981.

[31] Reddy JN. Mechanics of Laminated Composite Plates and Shells: Theory and Analysis. Boca Raton: CRC Press; 2004.

[32] Lee J. Center of gravity and shear center of thin-walled open-section composite beams. Composite Structures, 2001; 52: 255-260.

[33] Turkalj G, Brnic J, Prpic-Orsic J. Large rotation analysis of elastic thin-walled beam-type structures using ESA approach. Computers & Structures, 2003; 81(18-19): 1851-1864.

[34] Timoshenko SP, Gere JM. Theory of Elastic Stability, 2nd ed., McGraw-Hill, New York; 1961.

[35] Bleich F. Buckling Strength of Metal Structures, McGraw-Hill, New York; 1952.

[36] Trahair NS. Flexural-Torsional Buckling of Structures, CRC Press INC, Boca Raton; 1993.

[37] MSC.Nastran. Quick Reference Guide, Santa Ana, CA: MSC Software Corporation; 2007.

Table 1: Material distribution schemes

Cross section	Bottom flange	Web	Top flange
I1	C 7-3	B 3-4-3	C 7-3
I2	B 3-4-3	B 3-4-3	B 3-4-3
M1	C 1-9	B 3-4-3	C 9-1
M2	C 9-1	B 3-4-3	C 1-9
C1	A	A	A
C2	B 3-4-3	B 3-4-3	B 3-4-3
C3	C 1-9	C 9-1	C 1-9

Table 2: Critical buckling loads (MN) of FG symetric section I-beam (Type-I1) with various values of power-law index for different boundary conditions.

BC	Method	Power-law index *p*									
		0	0.25	0.5	1	2	5	10	20	30	50
C-F	Present	0.105773	0.101484	0.098626	0.095057	0.091494	0.087936	0.086321	0.085400	0.085073	0.084804
	Formula	0.105770	0.101480	0.098623	0.095055	0.091491	0.087933	0.086319	0.085397	0.085070	0.084801
S-S	Present	0.423296	0.406130	0.394692	0.380412	0.366150	0.351914	0.345451	0.341762	0.340455	0.339377
	Formula	0.423079	0.405921	0.394492	0.380218	0.365963	0.351733	0.345275	0.341588	0.340280	0.339203
C-C	Present	1.705050	1.635900	1.589830	1.532310	1.474860	1.417520	1.391480	1.376630	1.371360	1.367020
	Formula	1.692320	1.623690	1.577970	1.520870	1.463850	1.406930	1.381100	1.366350	1.361120	1.356810
C-S	Present	0.867292	0.832121	0.808686	0.779427	0.750207	0.721037	0.707795	0.700237	0.697558	0.695351
	Formula	0.863427	0.828411	0.805085	0.775955	0.746863	0.717823	0.704643	0.697118	0.694449	0.692252

Table 3: Critical buckling loads (MN) of FG symetric section I-beam (Type-I2) with various values of power-law index for different boundary conditions.

BC	Method	Power-law index *p*									
		0	0.25	0.5	1	2	5	10	20	30	50
C-F	Present	0.105773	0.097239	0.091552	0.084447	0.077346	0.070252	0.067030	0.065189	0.064536	0.063998
	Formula	0.105770	0.097236	0.091549	0.084444	0.077344	0.070249	0.067027	0.065187	0.064534	0.063996
S-S	Present	0.423296	0.389143	0.366385	0.337951	0.309533	0.281143	0.268247	0.260881	0.258268	0.256116
	Formula	0.423079	0.388945	0.366198	0.337777	0.309375	0.280998	0.268109	0.260747	0.258136	0.255985
C-C	Present	1.705050	1.567480	1.475810	1.361280	1.246810	1.132450	1.080500	1.050840	1.040310	1.031640
	Formula	1.692320	1.555780	1.464790	1.351110	1.237500	1.123990	1.072440	1.042990	1.032540	1.023940
C-S	Present	0.867292	0.797316	0.750687	0.692428	0.634203	0.576034	0.549611	0.534520	0.529165	0.524757
	Formula	0.863427	0.793765	0.747342	0.689340	0.631377	0.573464	0.547161	0.532137	0.526808	0.522419

Table 4: Critical buckling loads (MN) of FG mono-symetric section I-beam (Type-M1) with various values of power-law index for different boundary conditions.

BC	Method	Power-law index *p*									
		0	0.25	0.5	1	2	5	10	20	30	50
C-F	Present	0.052332	0.050180	0.048729	0.046930	0.045205	0.043629	0.042968	0.042596	0.042536	0.042353
	Formula	0.052330	0.050178	0.048728	0.046929	0.045204	0.043628	0.042967	0.042596	0.042463	0.042352
S-S	Present	0.155349	0.144328	0.136891	0.127638	0.118651	0.110139	0.106384	0.104208	0.103874	0.102754
	Formula	0.155292	0.144278	0.136845	0.127596	0.118614	0.110107	0.106354	0.104179	0.103388	0.102727
C-C	Present	0.420964	0.383527	0.358293	0.324033	0.294570	0.262352	0.247406	0.238651	0.237099	0.232848
	Formula	0.418531	0.381327	0.356252	0.324681	0.292941	0.260946	0.246105	0.237413	0.234270	0.231651
C-S	Present	0.255919	0.234569	0.220232	0.202353	0.184725	0.167473	0.159639	0.155067	0.154281	0.152025
	Formula	0.255114	0.233846	0.219565	0.201753	0.184195	0.167015	0.159215	0.154662	0.153012	0.151635

Table 5: Buckling loads (MN) of FG mono-symetric section I-beam (Type-M2) with various values of power-law index for different boundary conditions.

BC	Method	Power-law index p									
		0	0.25	0.5	1	2	5	10	20	30	50
C-F	Present	0.052332	0.046463	0.042630	0.037955	0.033421	0.029001	0.027003	0.025854	0.025444	0.025105
	Formula	0.052330	0.046424	0.042576	0.037895	0.033374	0.028987	0.027010	0.025876	0.025471	0.025137
S-S	Present	0.155349	0.138807	0.128300	0.115769	0.104056	0.092762	0.087610	0.084597	0.083509	0.082602
	Formula	0.155292	0.138479	0.127843	0.115282	0.103550	0.092452	0.087454	0.084549	0.083502	0.082631
C-C	Present	0.420964	0.387808	0.366821	0.340244	0.318037	0.294766	0.283972	0.277599	0.275284	0.273353
	Formula	0.418531	0.385040	0.363451	0.337323	0.312052	0.287181	0.275686	0.268936	0.266492	0.264455
C-S	Present	0.255919	0.231901	0.216730	0.198377	0.181816	0.165458	0.157931	0.153497	0.151888	0.150545
	Formula	0.255114	0.230782	0.215368	0.197088	0.179877	0.163409	0.155918	0.151537	0.149951	0.148629

Table 6: Critical buckling loads (MN) of FG chanel-section beam (Type-C1) with various values of power-law index for different boundary conditions.

BC	Method	Power-law index p									
		0	0.25	0.5	1	2	5	10	20	30	50
C-F	Present	0.264038	0.227681	0.203605	0.173752	0.144258	0.115272	0.102321	0.094998	0.092415	0.090293
	Formula	0.264029	0.227674	0.203598	0.173745	0.144253	0.115268	0.102318	0.094995	0.092412	0.090290
S-S	Present	0.780153	0.671251	0.601903	0.518922	0.438979	0.357429	0.316213	0.289897	0.279841	0.271209
	Formula	0.779838	0.669818	0.599930	0.516545	0.436609	0.355683	0.315064	0.289199	0.279324	0.270849
C-C	Present	2.648370	2.289850	2.053970	1.762670	1.474170	1.183630	1.047040	0.966028	0.936513	0.911828
	Formula	2.629830	2.269880	2.033740	1.743080	1.456660	1.170200	1.036450	0.957402	0.928654	0.904635
C-S	Present	1.427730	1.232280	1.105210	0.950041	0.797849	0.643889	0.569606	0.524308	0.507495	0.493287
	Formula	1.422100	1.225290	1.097690	0.942362	0.790781	0.638536	0.565575	0.521223	0.504784	0.490901

Table 7: Critical buckling loads (MN) of FG chanel-section beam (Type-C2) with various values of power-law index for different boundary conditions.

BC	Method	Power-law index p									
		0	0.25	0.5	1	2	5	10	20	30	50
C-F	Present	0.264038	0.242770	0.228595	0.210880	0.192919	0.170115	0.161249	0.156653	0.155106	0.153866
	Formula	0.264029	0.242763	0.228588	0.210872	0.192915	0.170112	0.161245	0.156649	0.155103	0.153863
S-S	Present	0.780153	0.702445	0.652023	0.591031	0.532957	0.478750	0.455684	0.442997	0.438583	0.434983
	Formula	0.779838	0.702153	0.651751	0.590777	0.532725	0.478538	0.455482	0.442801	0.438389	0.434791
C-C	Present	2.648370	2.419840	2.268920	2.082400	1.898890	1.719390	1.639420	1.594220	1.578280	1.565190
	Formula	2.629830	2.402790	2.252870	2.067590	1.885330	1.707060	1.627660	1.582790	1.566960	1.553960
C-S	Present	1.427730	1.297670	1.212370	1.107830	1.006260	0.908619	0.865831	0.841881	0.833472	0.826583
	Formula	1.422100	1.292490	1.207500	1.103330	1.002140	0.904875	0.862260	0.838408	0.830035	0.823174

Table 8: Critical buckling loads (MN) of FG chanel-section beam (Type-C3) with various values of power-law index for different boundary conditions.

BC	Method	Power-law index p									
		0	0.25	0.5	1	2	5	10	20	30	50
C-F	Present	0.264038	0.250473	0.240894	0.228250	0.214789	0.200467	0.193675	0.188398	0.186161	0.184240
	Formula	0.264029	0.250465	0.240887	0.228242	0.214782	0.200460	0.193669	0.189714	0.188298	0.187128
S-S	Present	0.780153	0.713228	0.669943	0.617496	0.566784	0.516814	0.493472	0.479555	0.474458	0.470180
	Formula	0.779838	0.712449	0.668922	0.616253	0.565433	0.515488	0.492210	0.478349	0.473275	0.469019
C-C	Present	2.648370	2.437160	2.296230	2.120400	1.945300	1.770760	1.691060	1.645100	1.628670	1.615070
	Formula	2.629830	2.418400	2.277560	2.102120	1.927820	1.754530	1.675580	1.630100	1.613850	1.600410
C-S	Present	1.427730	1.310760	1.233610	1.138390	1.044560	0.951420	0.908542	0.883514	0.874486	0.866975
	Formula	1.422100	1.304670	1.227340	1.132050	1.038360	0.945600	0.902991	0.878151	0.869195	0.861748

Table 9: Verification results for lateral buckling moments and loads of isotropic (ceramic) simply-supported beams.

	Pure bending, M (kNm)		Central point load, F (N)		Uniformly distributed load, q (kN/m)	
Section	Present	Closed-form [35]	Present	Closed-form [35]	Present	Closed-form [36]
I	10.0329	10.0986	6863.59	6946.90	1.4276	1.4401
M	5.49064	5.53538	4110.41	4169.04	0.84160	0.85342
C	16.8339	16.9274	11520.5	11510.7	2.39423	2.39465

Table 10: Critical buckling loads (MN) of L-shaped frame (Types - C2 and C3) with various values of power-law index for different boundary conditions.

Beam type	Load direction	Power-law index p									
		0	0.25	0.5	1	2	5	10	20	30	50
C2	(-) F	0.021267	0.019356	0.018099	0.016554	0.015048	0.013595	0.012956	0.012598	0.012472	0.012369
	(+) F	0.023729	0.021584	0.020175	0.018445	0.016760	0.015138	0.014425	0.014027	0.013886	0.013772
C3	(-) F	0.021267	0.020083	0.019285	0.018278	0.017257	0.016203	0.015699	0.015397	0.015287	0.015194
	(+) F	0.023729	0.022419	0.021539	0.020433	0.019313	0.018160	0.017608	0.017277	0.017156	0.017054

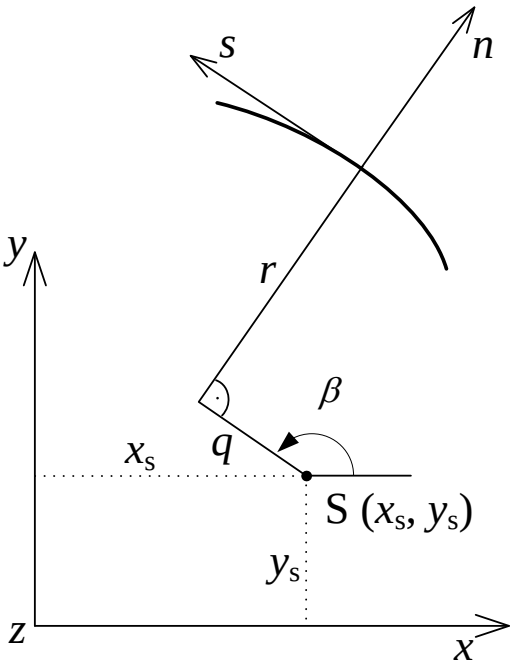

Fig.1. Contour coordinate system

FG wall (Type A) FG sandwich wall (Type B) FG sandwich wall (Type C)

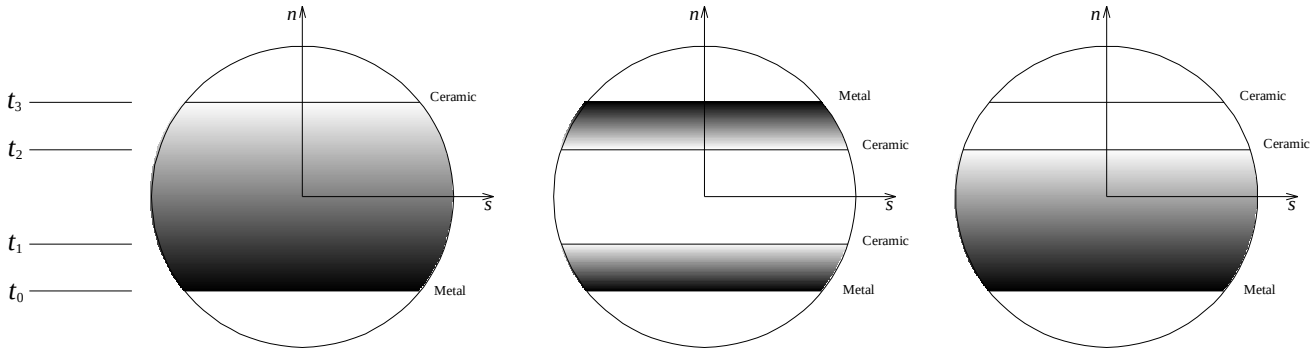

Fig. 2. Three types of beam walls (Types A, B and C).

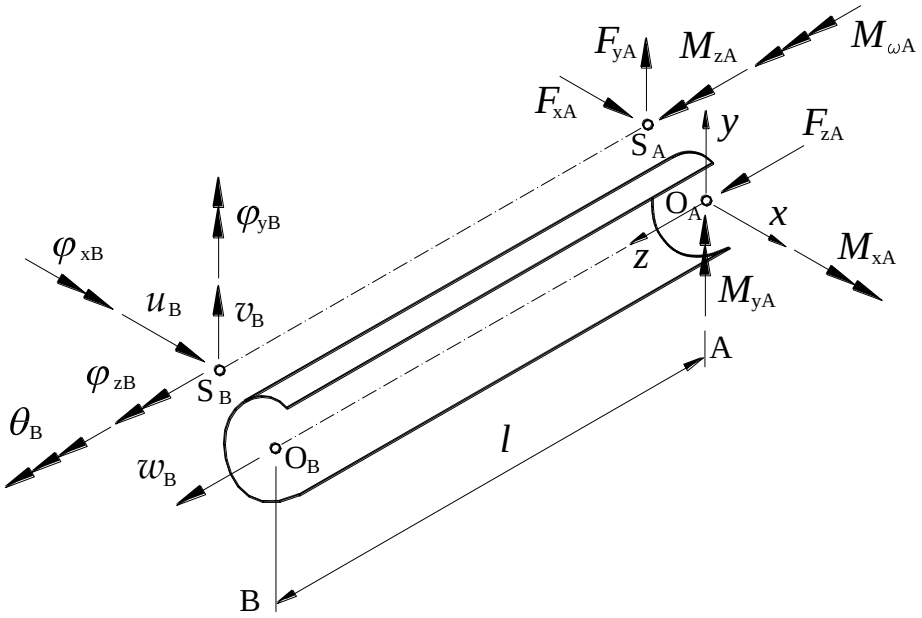

Fig. 3. 14-DOF beam element: nodal displacements and nodal forces.

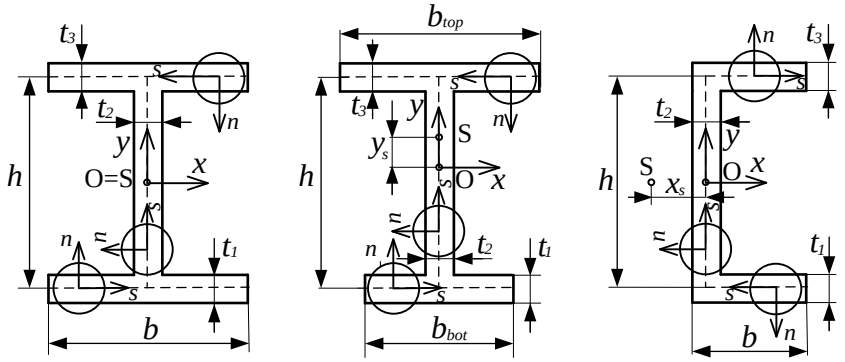

I M C

Fig. 4. Three types of thin-walled profiles.

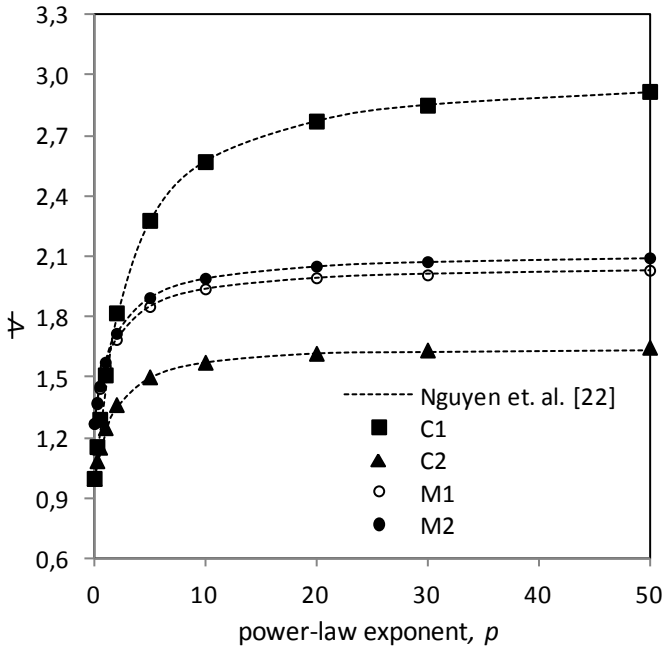

Fig. 5. Non-dimensional deflection of cantilevered beams types M1, M2, C1 and C2

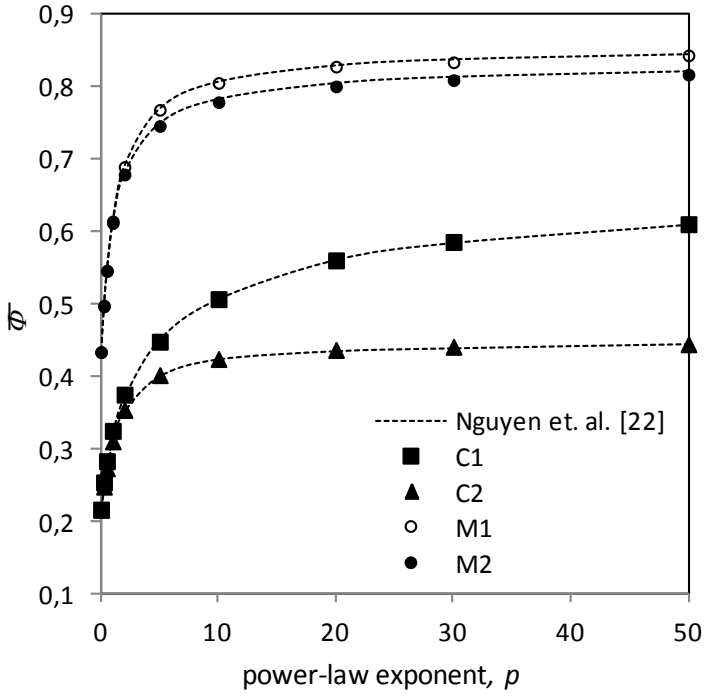

Fig. 6. Non-dimensional twist angles of cantilevered beams types M1, M2, C1 and C2

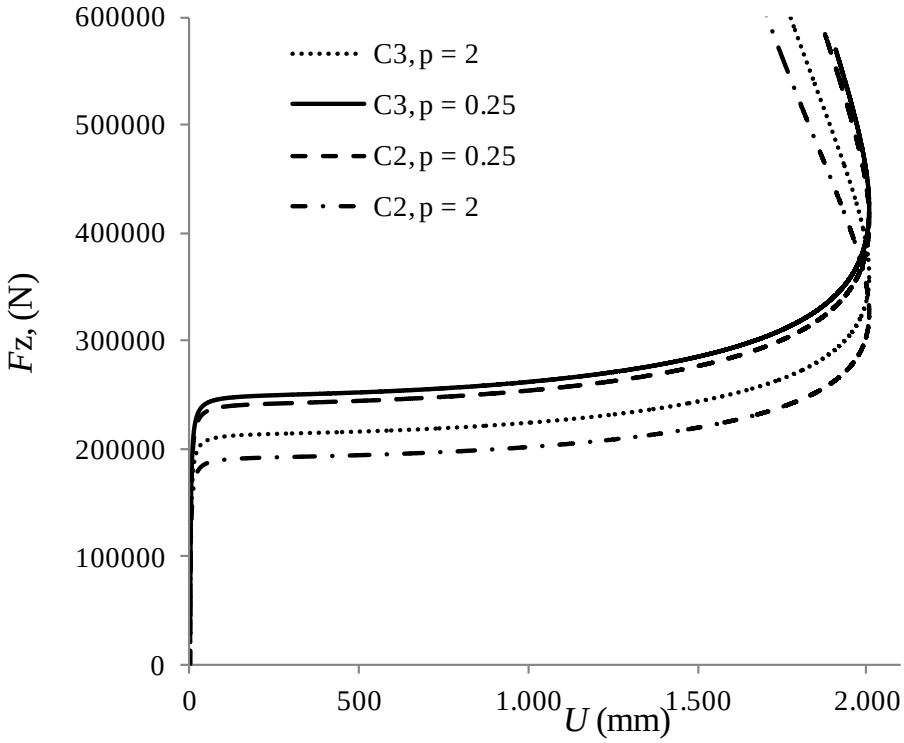

Fig. 7. Load vs. displacement with the power-law index values $p = 0.25$ and $p = 2$ for C2 and C3 cantilever beams

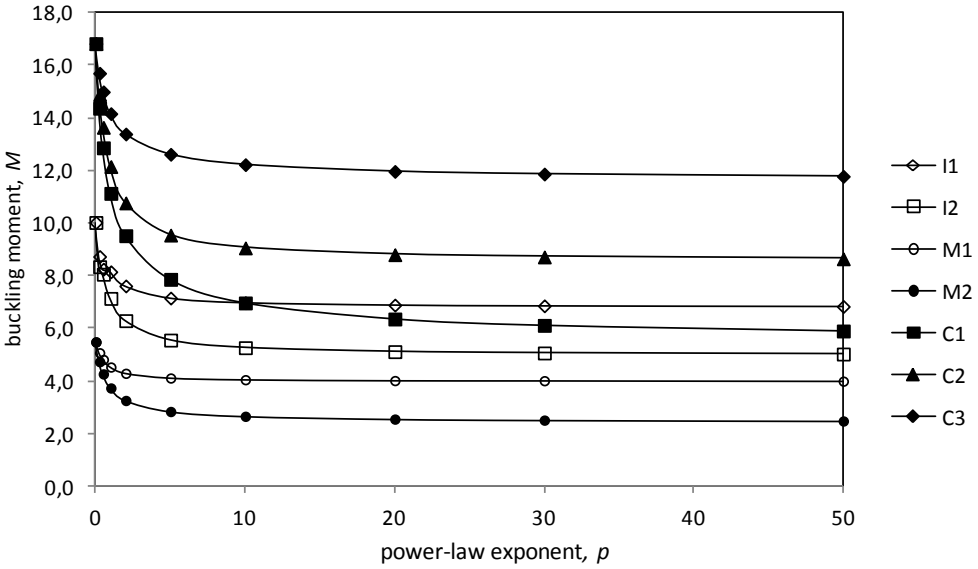

Fig. 8. Lateral buckling moment vs. power-law index for S-S beams under pure bending.

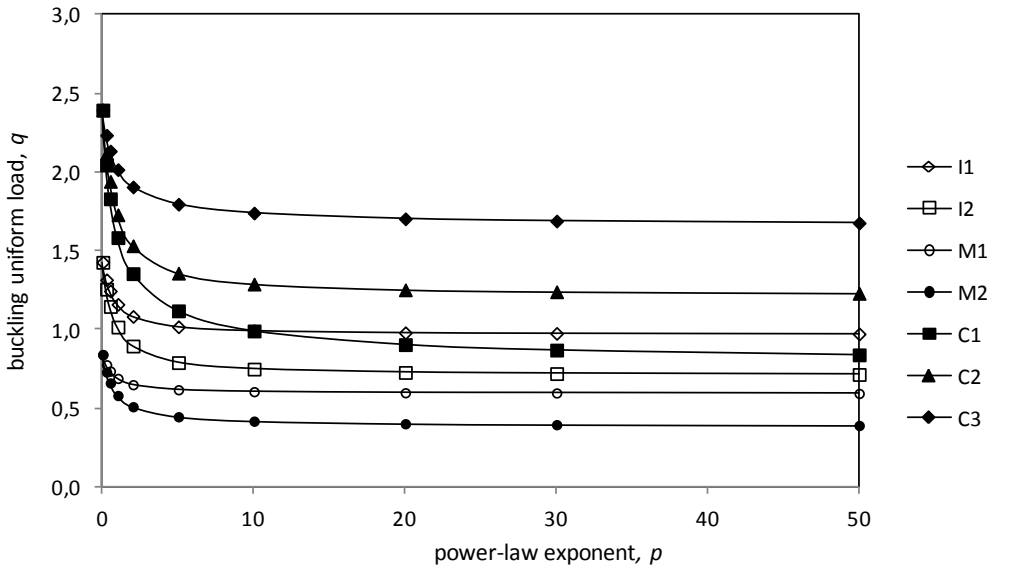

Fig. 9. Lateral buckling load vs. power-law index for S-S beams under uniform load.

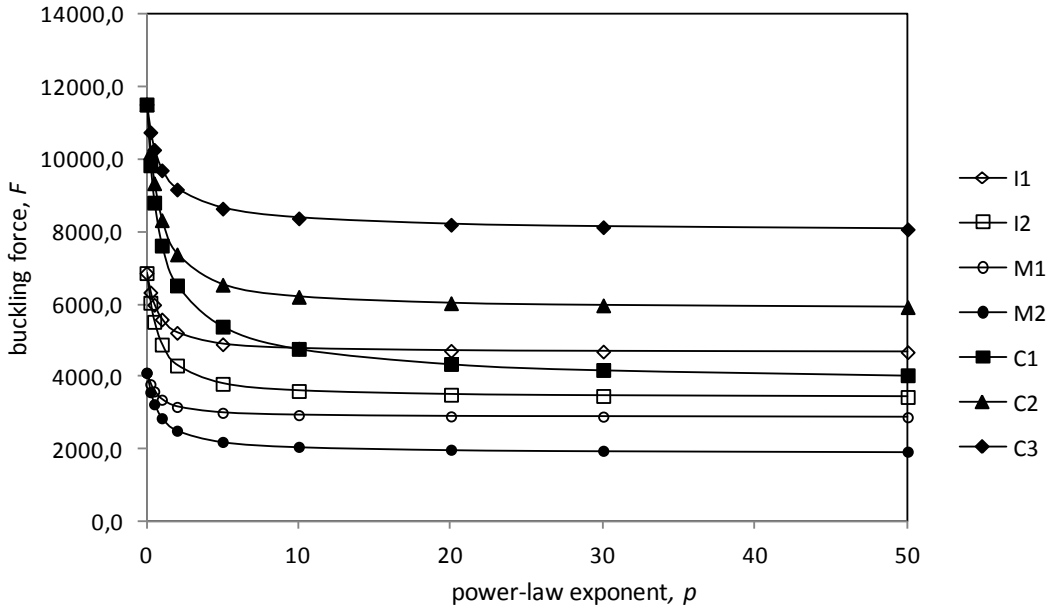

Fig. 10. Lateral buckling load vs. power-law index for S-S beams under central point load

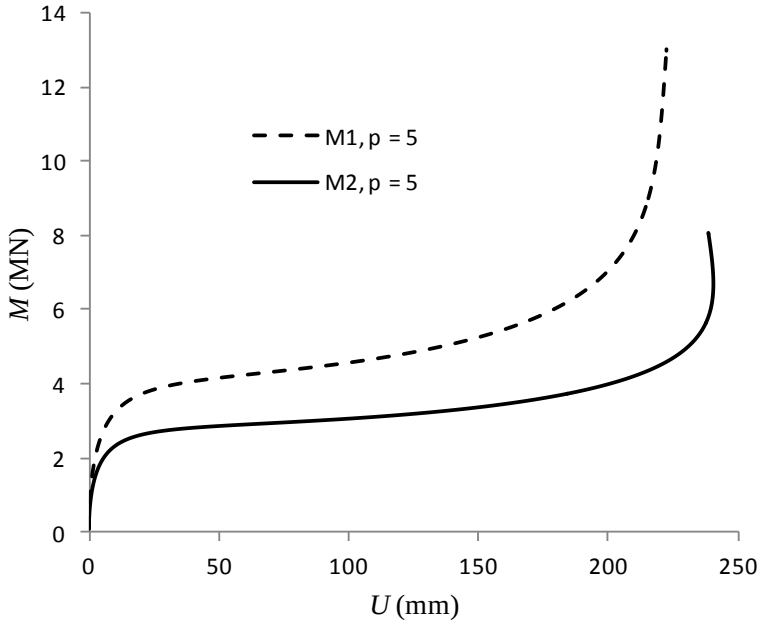

Fig. 11. Lateral displacement vs. applied moment M for M1 and M2 beams, $p = 5$

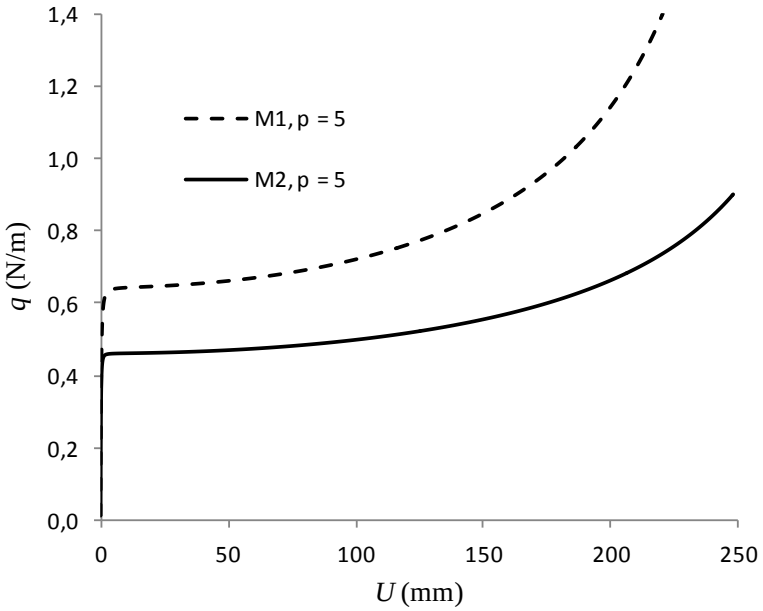

Fig. 12. Lateral displacement vs. applied uniform load q for M1 and M2 beams, $p = 5$

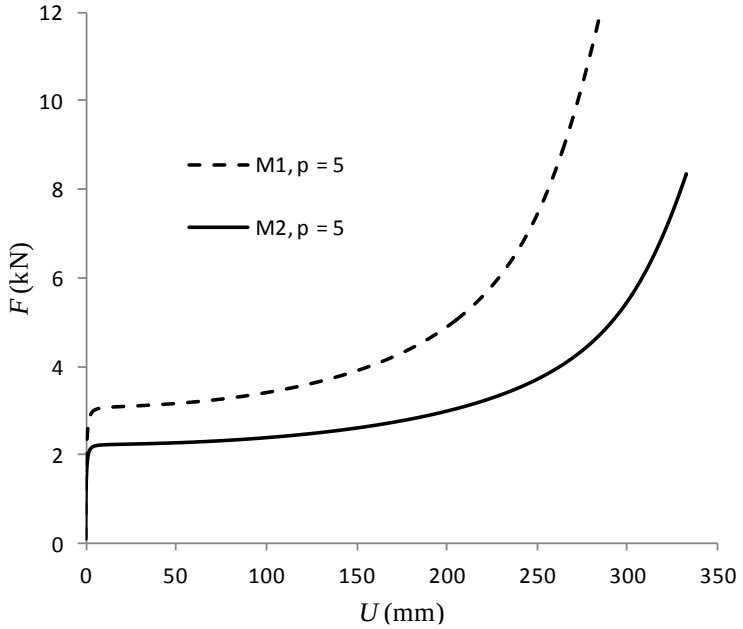

Fig. 13. Lateral displacement vs. applied force *F* for M1 and M2 beams, *p* = 5

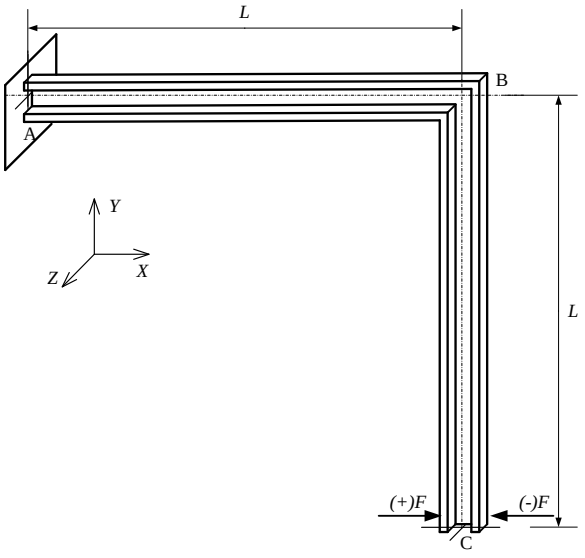

Fig. 14. *L*-shaped frame.

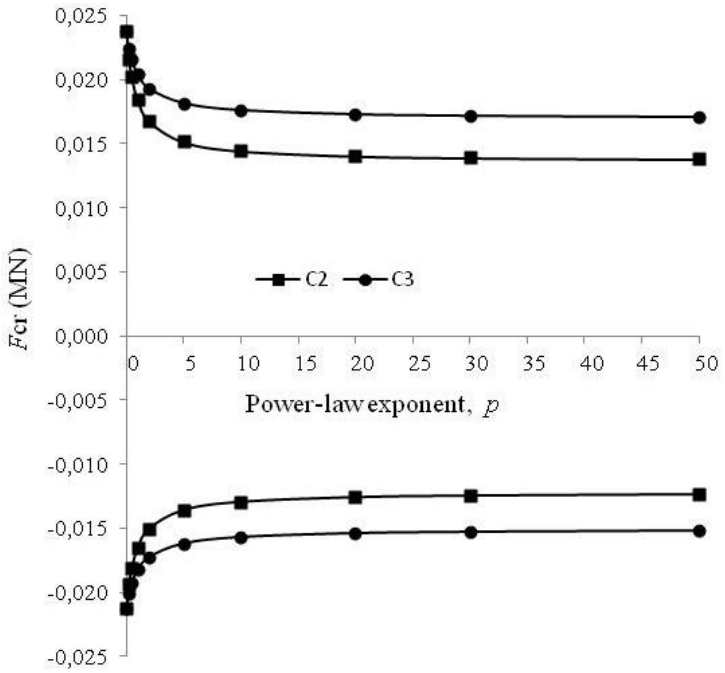

Fig. 15. Lateral buckling loads (MN) of L-cantilever (Types-C2 and C3) with various values of power-law index.

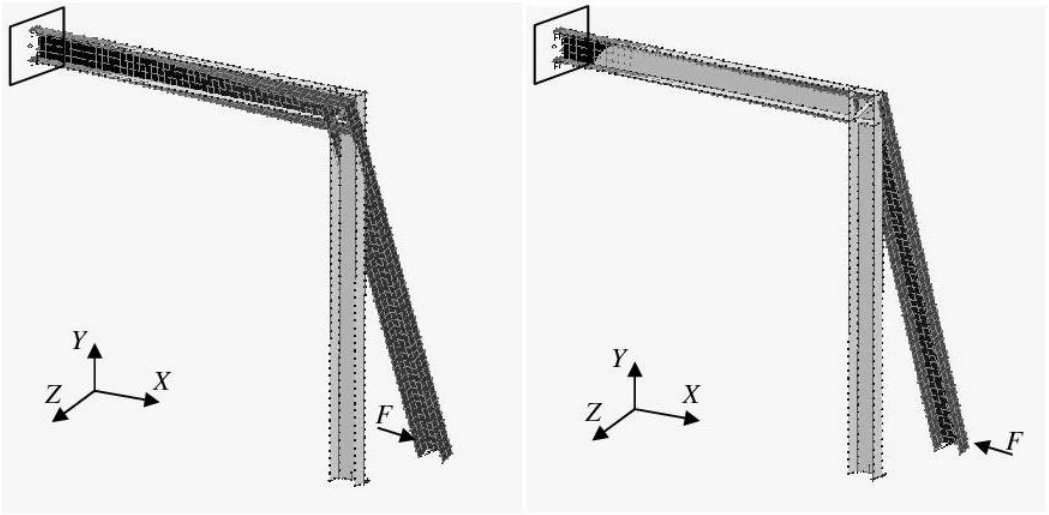

(a) F_{cr} = 22895 N (b) F_{cr}= 21184 N

Fig. 16. Lateral buckling modes of L-frame for two load direction using shell model in MSC.Nastran

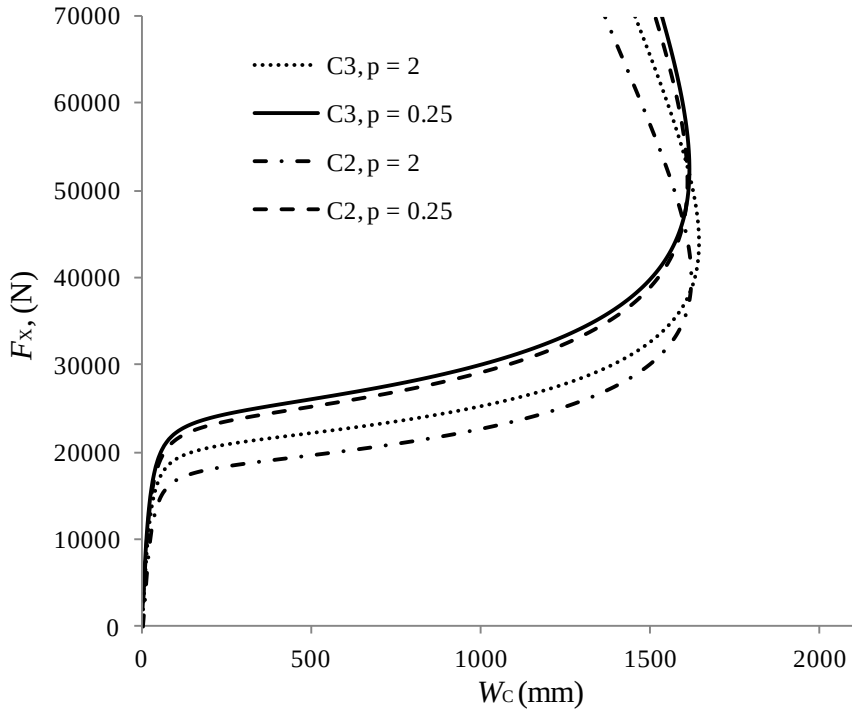

Fig. 17. Load vs. displacement of C2 and C3 L-frame under load *F* applied in (+) direction with the power-law index values $p = 0.25$ and $p = 2$

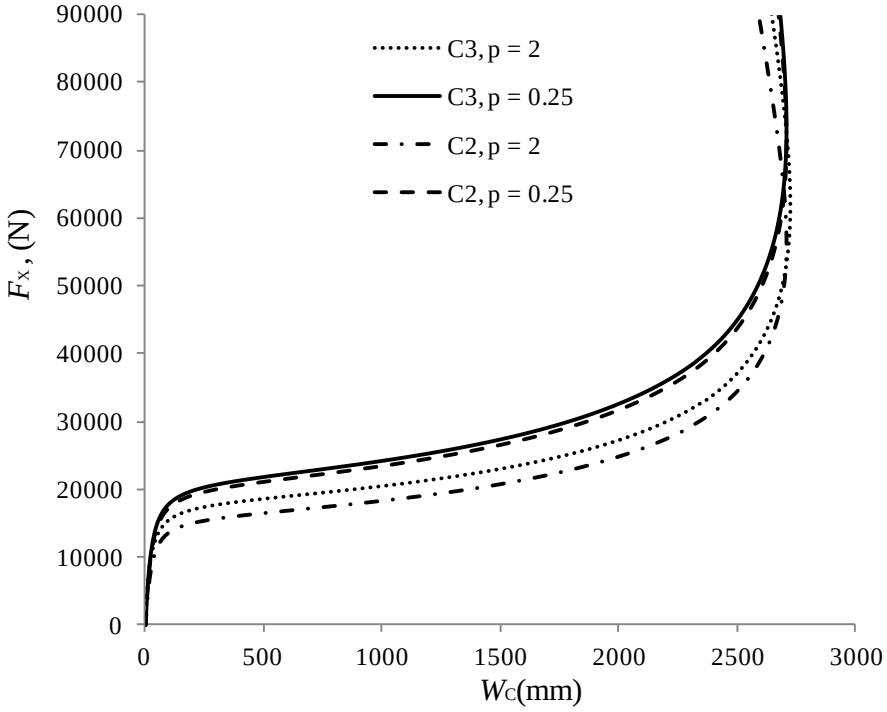

Fig. 18. Load vs. displacement of C2 and C3 L-frame under load *F* applied in (-) direction with the power-law index values $p = 0.25$ and $p = 2$